International Journal of Nanomedicine

Dovepress
Taylor & Francis Group

Open Access Full Text Article

ORIGINAL RESEARCH

Mesoporous Silica-Encapsulated Cerium Oxide Nanozymes and Quercetin for Synergistic ROS-Modulated Downregulation of Inflammatory Cytokines

Shanlei Zhou[1], Yu Zhang[1], Eudald Casals[2], Muling Zeng[3], Manuel Morales-Ruiz[4,5], Qingshi Liu[6], Bo Zhang[7], Gregori Casals[4,8]

[1]Department of Endocrinology, The First Affiliated Hospital of Anhui Medical University, Hefei, 230022, People's Republic of China; [2]Premium Research SL, Guadalajara, 19003, Spain; [3]Materials Science Institute of Barcelona (ICMAB-CSIC), Bellaterra, 08193, Spain; [4]CDB, Hospital Clínic of Barcelona, IDIBAPS, CIBEREHD, Barcelona, Spain; [5]Department of Biomedicine, Faculty of Medicine and Health Science, University of Barcelona, Barcelona, 08036, Spain; [6]State Key Laboratory of Rare Earth Resources Utilization, Changchun Institute of Applied Chemistry, Chinese Academy of Sciences, Changchun, 130022, People's Republic of China; [7]The First Clinical Medical College of Anhui University of Chinese Medicine, Hefei, 230031, People's Republic of China; [8]Department of Fundamental and Clinical Nursing, Faculty of Nursing, University of Barcelona, L'Hospitalet de Llobregat, 08907, Spain

Correspondence: Qingshi Liu; Bo Zhang, Email qsliu@ciac.ac.cn; 13956934348@139.com

Introduction: Combining natural antioxidants with nanozymes represents a promising strategy to enhance therapeutic outcomes in oxidative stress-related diseases. This study integrates quercetin (Que), a plant-derived flavonoid with strong antioxidant activity, and cerium oxide nanozymes (CeO_2NZs) into mesoporous silica ($mSiO_2$) to enhance therapeutic efficacy and overcome the poor solubility and bioavailability of natural antioxidants.

Methods: Large-pore $mSiO_2$ (11 nm) were synthesized via a sol–gel method to encapsulate cerium oxide nanozymes (CeO_2NZs). Que was loaded using solvent impregnation to obtain (CeO_2/Que)@$mSiO_2$ nanocomposites. Structural and chemical characterization was performed, and biological evaluations were conducted in A549 cells.

Results: The incorporation of a large mesopore $mSiO_2$ (11 nm) significantly enhanced Que loading capacity and its sustained release in cell culture media. The (CeO_2/Que)@$mSiO_2$ nanocomposite demonstrated excellent biocompatibility, effective ROS scavenging, and significant downregulation of inflammatory cytokines (IL-1β, IL-6, TNF-α) compared to free Que.

Conclusion: The (CeO_2/Que)@$mSiO_2$ nanoplatform offers synergistic antioxidant and anti-inflammatory effects, supporting its potential for treating oxidative stress-related inflammatory conditions.

Keywords: quercetin, cerium oxide nanoparticles, nanozymes, oxidative stress, chronic inflammation

Introduction

Oxidative stress results from the excessive accumulation of reactive oxygen species (ROS) that overwhelm cellular antioxidant defenses. This imbalance damages critical biomolecules such as DNA, proteins, and lipids, leading to cellular dysfunction and activation of inflammatory signaling pathways. While the immune response aims to promote tissue repair and pathogen clearance, persistent ROS elevation and chronic inflammation cause sustained tissue injury, disruption of cellular homeostasis, and contribute to the development of numerous diseases, including neurodegenerative disorders, cancer, cardiovascular diseases, and autoimmune conditions.

Quercetin (Que), a naturally occurring flavonoid, has emerged as a promising candidate for addressing oxidative stress-related diseases, such as chronic inflammation, due to its potent antioxidant and anti-inflammatory properties.[1–5] These therapeutic effects are derived from Que's ability to scavenge reactive oxygen species (ROS) and modulate several inflammatory pathways that mitigate the detrimental effects of oxidative stress.[6–9] Despite these benefits, and common to

Received: 9 March 2025
Accepted: 17 June 2025
Published: 25 June 2025

Graphical Abstract

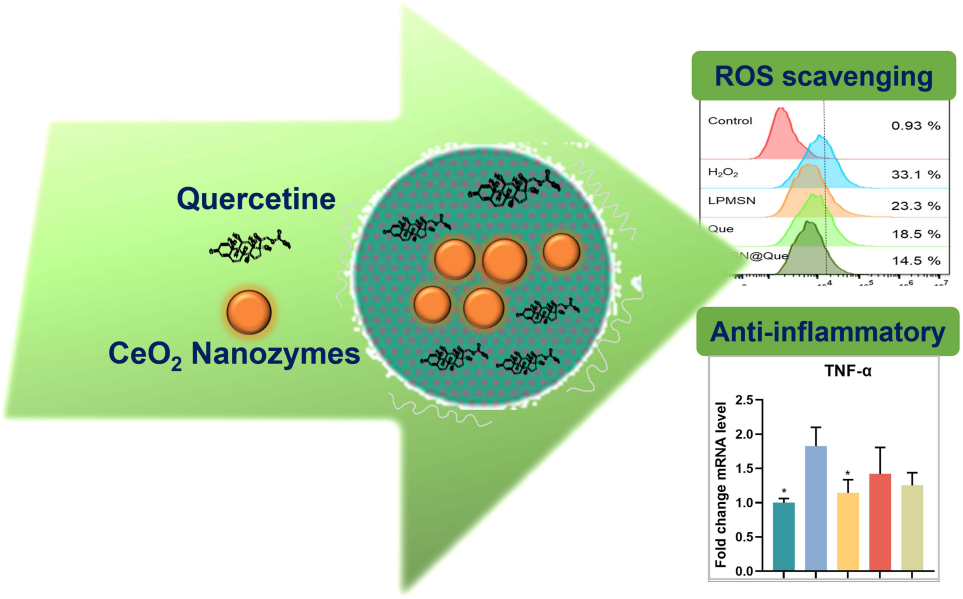

other natural flavonoids, the clinical application of Que remains limited due to its poor water solubility, which reduces its bioavailability,[10,11] and its rapid degradation and systemic clearance.[1,12,13] All this makes it necessary to explore innovative delivery systems to optimize Que's pharmaceutical potential.

To address these limitations, advanced drug delivery systems have been developed using nanocarriers such as mesoporous silica nanoparticles ($mSiO_2$), liposomes, and micelles.[14–16] These structures protect therapeutic agents from premature degradation, enhance their stability, and facilitate their targeted release at the desired site of action, thereby improving the therapeutic efficacy of poorly soluble drugs. Different studies have shown controlled and sustained Que release profiles by employing advanced nanocarriers, such as silica[17] and $mSiO_2$,[18,19] chitosan-stabilized liposomes,[20] chitosan-carbon nanotube composites,[21] polymeric micelles,[16] hyaluronic acid nanomicelles,[22] triblock copolymers,[23] among others. And recent reviews provide detailed literature on the use of nanoscale agents for the delivery of Que, especially for applications in cancer treatment.[24,25] However, the limited duration of therapeutic effect still remains a concern.

However, another limitation of the clinical potential of Que, and other natural antioxidants, is that while its ROS-scavenging activity plays a key role in alleviating oxidative stress[6,26–29] (Figure 1), this alone is insufficient to effectively manage chronic inflammatory conditions. Chronic inflammation often requires sustained therapeutic interventions, which natural antioxidants like Que may fail to provide due to their susceptibility to deactivation and the need for repeated dosing.[30–32]

A promising approach to overcome this limitation, is the combination of natural antioxidants like Que with synthetic nanozymes (NZs), nanomaterials with enzyme-like catalytic activity that have emerged as a targeted and effective approach for mitigating ROS-related damage.[34–36] With their robust and sustained catalytic activity, NZs can complement natural compounds like Que by providing long-lasting protection against ROS and supporting inflammation regulation over extended periods.[37,38] This combination strategy enhances therapeutic outcomes, making it particularly relevant for chronic inflammatory conditions. For instance, a recent study by Zhang et al prepared a flavonoid-rich sesame leaf extract (SLE) containing 83 identified flavonoids and used it to synthesize iron (Fe)-based NZs (Fe-SLE CPNs), demonstrating enhanced ROS scavenging, anti-inflammatory effects via MyD88-NF-κB-MAPK pathway modulation, and robust stability in different physiological conditions.[39]

In this study, the limitations of Que delivery and activity have been addressed by developing a core-shell nanocarrier based on a mshell encapsulating both Que and Cerium oxide NZs (CeO_2NZs), widely explored for their multi-enzymatic

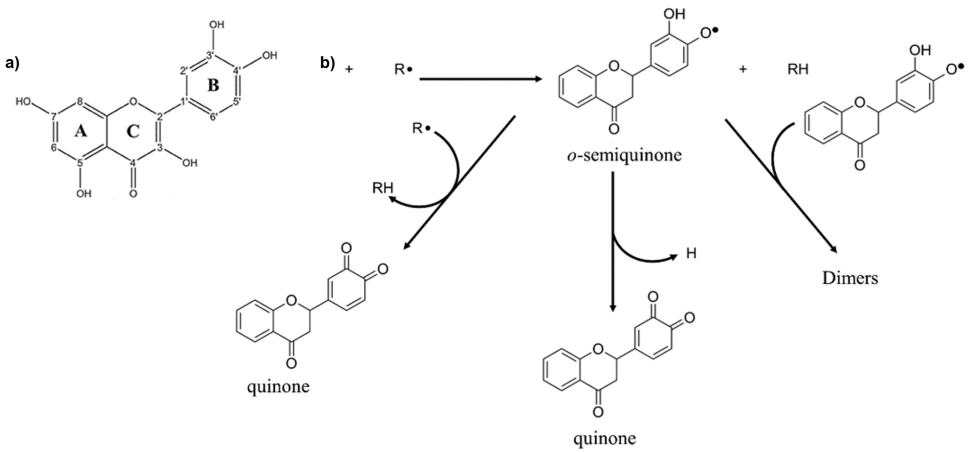

Figure 1 Que mechanism of action. (**a**) Chemical structure of Que. (**b**) The mechanism by which flavonoids scavenge ROS begins with the reduction of the free radical (R•) to R-H, which is accompanied by the oxidation of the flavonoid into a flavonoid radical. This flavonoid radical can follow one of three pathways: it may reduce another free radical to form a quinone, donate a hydrogen atom to produce a quinone (resulting in the loss of quercetin's antioxidant activity), or pair with another flavonoid radical to form a dimer, significantly diminishing its ability to donate electrons or hydrogen atoms. Hence, the need to explore novel therapeutic strategies that combine Que's potent activity with more sustained mechanisms of action. Reproduced from Slike et al Biomed. Pharmacother. 146, 112,442, 2022,[33] under a Creative Commons Attribution-NonCommercial-NoDerivatives 4.0 International License.

mimetic activities.[40–45] The development of such advanced drug delivery systems aligns with the growing interest in synergistic bio- and nanoparticle-based formulations for therapeutic applications. Beyond drug delivery, this $mSiO_2$-based platform facilitates the incorporation of NZs and natural products into eg wound dressings, enabling localized therapeutic applications such as skin regeneration and wound healing.[46,47] The combination of CeO_2NZs and Que within the nanocarrier enhances stability, bioavailability, and therapeutic efficacy, providing sustained Que release and the essential antioxidant and anti-inflammatory properties for such tissue repair.[48]

To the best of our knowledge, this represents a novel strategy for encapsulating both natural and synthetic therapeutic agents within an $mSiO_2$ shell. Previous approaches aimed to achieve similar synergistic effects by immobilizing Que in CeO_2 bound to albumin,[49] embedding Que in mesoporous CeO_2,[50] or incorporating Que into complexes with other structures such as polymers.[8] The CeO_2@$mSiO_2$ core-shell structures were synthesized using a sol–gel method combined with pore-expanding strategies to optimize their drug loading and release capacity. Que was loaded into the nanocarriers via solvent impregnation to produce the final (CeO_2/Que)@$mSiO_2$ nanocomposites. The large mesopore size of 11 nm significantly enhanced Que's loading efficiency and facilitated controlled release in physiological environments, such as cell culture media. Biological evaluations demonstrated that (CeO_2/Que)@$mSiO_2$ exhibits excellent biocompatibility, high ROS-scavenging capacity, and potent anti-inflammatory activity, as evidenced by reduced ROS levels and downregulated expression of inflammatory genes. These findings highlight the potential of combining natural antioxidants like Que with synthetic NZs to develop effective strategies for managing chronic inflammation and oxidative stress-related diseases.

Materials and Methods

Reagents and Chemicals

For the synthesis of the (CeO_2/Que)@MSNs nanocomposite, cerium (III) nitrate hexahydrate, methanol, anhydrous ethanol, sodium chloride, tetraethyl orthosilicate (TEOS), and hexadecyltrimethylammonium bromide (CTAB) were obtained from Aneji Chemicals (Sane Chemical Technology, Shanghai, China). Concentrated ammonia water (28–30 wt %) was supplied by Acros Organic (Thermo Fisher Scientific, China), while ammonium nitrate was procured from Guangdong Shantou Xilong Chemical Plant (XL). Decane was purchased from Aladdin (Shanghai Aladdin Biochemical Technology Co., Ltd.), and mesitylene (1,3,5-trimethylbenzene) and quercetin were sourced from Sigma-Aldrich (Shanghai) Trading Co., Ltd.

Additional reagents for cell culture and antioxidant activity assays included RPMI 1640, fetal bovine serum (FBS), penicillin–streptomycin mixture, 0.25% trypsin-EDTA, and PBS pH 7.4 buffer, all obtained from Gibco (Thermo Fisher

 https://doi.org/10.2147/IJN.S525411

Scientific Biochemicals Co., Ltd., and Shanghai Biyuntian Biotechnology Co., Ltd.). MTT and the reactive oxygen species detection kit were procured from Blue Sky (Shanghai Bio-Tech Co., Ltd.), while dimethyl sulfoxide (DMSO) was from Sigma-Aldrich (Shanghai Trading Co., Ltd.). Isopropyl alcohol was supplied by Aladdin (Shanghai Aladdin Biochemical Technology Co., Ltd.), and chloroform and 30% hydrogen peroxide were obtained from Guangzhou Chemical Reagent Factory. DEPC water was purchased from Biosharp (Beijing Lanjieke Technology Co., Ltd.).

For molecular biology experiments, Trizol reagent for total RNA extraction and the StarScript III Reverse Transcription Kit were obtained from Blue Sky (Shanghai Bio-Tech Co., Ltd.). and Genestar (Beijing Kangrun Chengye Biotechnology Co., Ltd.), respectively. The 2× RealStar Fast Dye Method qPCR Master Mix was also sourced from Genestar.

Synthesis of the CeO_2@MSNs Core-Shell Nanoparticles

A total of 120 mg of CTAB was dissolved in 4 mL of an ethanol-water solution (4:1, v/v H_2O/EtOH), and this solution was slowly added dropwise to 35.2 mL of CeO_2 nanoparticles (6.7 mM) in an ethanol-water solution (3.9:1, v/v H_2O/EtOH) under ultrasonic conditions. The pH of the resulting mixture was adjusted to approximately 10 by adding 160 μL of concentrated ammonia solution (28–30 wt%). Following 15 minutes of ultrasonication, 330 μL of decane was added slowly under stirring at room temperature and atmospheric pressure, and 92 μL of TMB was introduced after stirring for 1.5 hours. The mixture was continuously stirred for an additional 2 hours, after which a solution of TEOS (280 μL) and ethanol (1.2 mL) was added dropwise while ultrasonication was performed for 2 minutes. Finally, the reaction mixture was stirred overnight, and the resulting nanoparticles were washed three times with 40 mL of saturated sodium chloride in methanol (NaCl-MeOH) under ultrasonic conditions to fully remove the template agent CTAB.

Loading and Release Studies

A concentration calibration curve for Que in anhydrous ethanol was prepared by measuring absorbance at 373 nm for solutions with concentrations ranging from 0.0025 mg/mL to 0.015 mg/mL. The resulting standard curve, with a linear equation of A = 84.32C - 0.020 (where A is the absorbance and C is the concentration in mg/mL), showed a good linear correlation ($R^2 = 0.998$) between Que concentration and absorbance in the 2.5–15 μg/mL range.

For the preparation of CeO_2/Que)@MSNs, a saturated ethanol solution of Que was mixed with ethanol solutions containing CeO_2@MSNs with the different pore diameters in a 1:1 (v/v) ratio. After 24 hours of stirring in the dark, the mixtures were centrifuged, and the precipitate was washed and re-ultrasonicated with ethanol to obtain the final nanocomposites. The drug loading efficiency and amount were calculated using the absorbance values obtained from the UV spectrophotometry measurements, referring to the calibration curve. The optimal drug loading ratio was determined by mixing a saturated quercetin solution (14.89 mg/mL) with CeO_2@MSNs (DP≈11 nm) in a 1:1 (v/v) ratio. Various mass ratios were tested (3:1, 2:1, 1:1, 1:2, and 1:3), and the results showed that the 3:1 ratio provided the highest drug loading efficiency and amount.

For release experiments, first, a saturated Que ethanol solution was mixed with either CeO_2@MSNs (DP≈11 nm) or CeO_2@MSNs (DP≈3 nm and 6 nm) at 3:1 v/v ratio in all cases to load the Que using the solvent impregnation method, as previously described. The prepared CeO_2/Que)@MSNs (larger and smaller pore size) were then dispersed in 15 mL of PBS buffer and the mixtures were stirred at 250 rpm at 37 ± 1°C in the dark. At different time points, 1 mL of the solution was collected and centrifuged (3 min, RCF 20,000, 4°C). To simulate in vivo release more accurately, 1 mL of fresh PBS was added each time a sample was collected. The absorbance of quercetin in the supernatant was measured at 370 nm using a UV spectrophotometer, and the Que concentration at each time point was calculated by referencing the concentration calibration curve of Que.

Characterization Techniques

The CeO_2@MSNs and (CeO_2/Que)@MSNs nanocomposites were characterized using a variety of techniques to assess their structural and chemical properties. Ultraviolet-Visible (UV-Vis) absorption spectroscopy was performed to obtain the absorbance spectrum of the samples over the 230 nm to 700 nm wavelength range. Dynamic Light Scattering (DLS) was employed to measure the hydration kinetic diameter of the nanoparticles by analyzing the light scattering intensity, with a detection temperature of 25°C and a light source wavelength of 532 nm. Transmission Electron Microscopy

(TEM) was used to obtain high-resolution images of the nanocomposites, with the CeO_2 cores showing uniform particle sizes around 4 nm. High-Angle Annular Dark-Field (HAADF) imaging and Elemental Mapping via Energy Dispersive X-ray Spectroscopy (EDS) were performed to provide detailed information on the surface morphology, elemental distribution, and the incorporation of CeO_2 into the mesoporous silica structure. X-ray Photoelectron Spectroscopy (XPS) was used to analyze the chemical state of Ce, revealing the mixed valence state of Ce^{4+} and Ce^{3+} in the composite. Brunauer–Emmett–Teller (BET) surface area analysis and Density Functional Theory (DFT)-based pore size distribution confirmed the presence of mesopores in the nanocomposites, with varying pore sizes depending on the synthesis conditions. Fourier Transform Infrared (FTIR) spectroscopy provided insight into the functional groups present in the nanocomposites, revealing interactions between the quercetin molecules and the mesoporous silica surface. Lastly, X-ray Diffraction (XRD) analysis confirmed the crystalline structure of CeO_2 and indicated that quercetin was incorporated into the mesoporous silica in an amorphous state. These combined characterization techniques confirm the successful synthesis and functionalization of the CeO_2/Que)@MSNs nanocomposites.

Cell Viability Assay

First, A549 cells obtained from ATCC (Beijing, China) were seeded in a 96-well plate at a density of 8,000 cells/well, with a culture medium volume of 100 μL/well and incubated for 24 hours. After incubation, the supernatant was removed, and serum-free culture medium containing the sample was added. Concentrations were set to 1.56 μg/mL, 6.25 μg/mL, 25 μg/mL, 50 μg/mL, and 100 μg/mL, with five replicate wells for each concentration. The plates were incubated at 5% CO_2 and 37°C for 24 hours. After incubation, the supernatant was removed, and the plates were washed with 100 μL/well of PBS buffer. Then, 100 μL of serum-free culture medium and 10 μL of 5 mg/mL MTT solution were added to each well, and the plates were incubated in the dark for 4 hours. Finally, the supernatant was removed, and 100 μL of DMSO was added to each well. The plate was then placed on a shaker (360 rpm, 10 min) to fully dissolve the blue-purple crystalline formazan. The absorbance of each well was measured at OD 490 nm using a multifunctional microplate reader.

ROS Level Detection

Cells were seeded in a 12-well plate at a density of 2×10^5 cells/well, with 1 mL of culture medium per well. After overnight incubation, the supernatant was removed, and each well was washed with PBS. Serum-free culture medium containing the sample was added and incubated for 2 hours, and H_2O_2 was added to induce oxidative stress in the cells. After incubation for the specified periods, the supernatant was removed, and the cells were washed three times with PBS buffer.

Next, 300 μL of 10 μM DCFH-DA probe solution was added to each well. After incubating for 25 minutes, each well was washed three times with PBS buffer to remove any unincorporated DCFH-DA probes. Finally, the cells were observed using an inverted fluorescence microscope, or they were digested with trypsin and collected for flow cytometry analysis.

Detection of Inflammatory Factor Gene Expression Levels

A549 cells were seeded at a density of 2×10^5 cells/well on a 12-well plate, with duplicate wells for each condition. After overnight incubation, each well was washed with of PBS buffer. Serum-free medium was added and incubated for 2 hours, followed by the addition of H_2O_2 to induce oxidative stress in the cells. After the incubation period, the supernatant was removed, and the cells were washed three times with pre-cooled PBS buffer. Next, 0.5 mL of Trizol reagent was added to each well to extract total RNA from the cells. The concentration and purity of the RNA were determined using a Nanodrop spectrophotometer. An A260/280 ratio between 1.8 and 2.0 indicated that the RNA sample was relatively pure and free of significant protein or other contaminants.

Next, 550 ng of the extracted RNA was reverse transcribed into cDNA, following the instructions provided in the kit. The resulting cDNA was then used for real-time fluorescence quantitative polymerase chain reaction (qPCR). The primers used for qPCR were as follows: IL-6 (F: 5′-ACTCACCTCTTCAGAACGAATTG-3′; R: 5′-CCATCTTTGGAAGGTTCAGGTTG-3′), TNF-α (F: 5′-AGCCCATGTTGTAGCAAACC-3′; R: 5′-TGAGGTACAGGCCCTCTGAT-3′), IL-1β (F: 5′-CCACGGCCACATTTGGTT-3′; R: 5′-AGGGAAGCGGTTGCTCATC-3′), and the internal reference gene β-Actin (F: 5′-AAAGACCTGTACGCCAACAC-3′; R: 5′-GTCATACTCCTGCTTGCTGAT-3′).

 https://doi.org/10.2147/IJN.S525411

Statistical Analysis

Quantitative data were evaluated using GraphPad Prism version 8 (GraphPad Software Inc., San Diego, CA, USA). To assess differences among multiple groups, a one-way analysis of variance (ANOVA) was conducted, followed by the Newman–Keuls post hoc test. Comparisons between two independent groups were analyzed using the unpaired Student's *t*-test. Results are presented as mean ± standard error of the mean (SEM), with statistical significance set at $p \leq 0.05$.

Results and Discussion

Synthesis and Characterization of the CeO_2@mSiO_2 Core-Shell Nanostructures

The synthesis of CeO_2@mSiO_2 was carried out following a previously reported method with modifications to expand pore size.[51] First, CeO_2 cores were synthesized via chemical precipitation using Cerium Nitrate as the Cerium source, with the pH adjusted to 11 using NH_4OH. TEM images of the CeO_2NZs revealed a uniform nanoparticle size of approximately 4 nm (Figure 2a). The Ce in the nanoparticles exhibited a mixed valence state, with a Ce^{4+}/Ce^{3+} ratio of approximately 72:28 (Figure 2b) and the UV spectrum displayed the characteristic Ce^{4+} absorption peak at 296 nm (Figure 2c). Further, to synthesize CeO_2@mSiO_2, the CeO_2 cores were dispersed in an ethanol-water solution, with cetyltrimethylammonium bromide (CTAB) as the template and tetraethyl orthosilicate (TEOS) as the silica source. Pore expansion was achieved by introducing 1,3,5-trimethylbenzene (TMB) and decane as pore expanders.

Experimental parameters, including the molar ratios of TEOS to CTAB, pore expanders to CTAB, ethanol-to-water volume ratios, and stirring times, were systematically optimized and three different samples were selected for further experiments, including CFigureeO$_2$@mSiO_2 nanoparticles synthesized without pore expanders (pore diameter (D_P) ≈ 3 nm and a hydrodynamic diameter (D_H) of 73.2 nm), CeO_2@mSiO_2 synthesized with pore expanders and treated with NH_4NO_3 for surfactant removal ($D_P \approx 6$ nm),[52] and using saturated NaCl in methanol for CTAB removal ($D_P \approx 11$ nm). Figure 2d and e show TEM images of these samples. Specifically, CTAB, serving as the structure-directing agent, was dissolved in a 4:1 ethanol-water solution (v/v H_2O/EtOH) and added dropwise to a 3.9:1 ethanol-water solution (v/v H_2O/EtOH) containing CeO_2 cores under sonication. The pH of the mixture was adjusted to 10 using NH_4OH. Following 15 minutes of sonication, decane was added slowly under stirring at room temperature and atmospheric pressure. After 1 hour, trimethylbenzene (TMB) was introduced into the mixture under continuous stirring. The reaction was stirred for an additional 2 hours, and then a solution of TEOS was added dropwise. The reaction mixture was stirred overnight, and the resulting core-shell nanoparticles were washed three times with 40 mL of saturated sodium chloride in methanol (NaCl-MeOH) under sonication to completely remove the CTAB template. Table 1 shows the different ratios of reagents employed in the syntheses and sample characteristics.

The experimental parameters above described were adjusted based on the pore expansion mechanisms of TMB and decane. TMB interacts with the surfactant's head group through a cation–π interaction, and its planar structure facilitates diffusion between the surfactant's alkyl chains. This creates a hydrophobic effect that increases micelle size. Additionally, TMB's interaction hinders the adsorption of TEOS on the surfactant head group, weakening local electrostatic forces between the N^+ of CTAB and TEOS and accelerating TEOS condensation. The hydrolysis of TEOS produces ethanol, which increases TMB solubility in the aqueous phase, allowing TMB to diffuse outward from the micelle's core, further enlarging the micelle size. In contrast, decane, as a linear hydrocarbon, remains concentrated in the micelle's hydrophobic region and expands pore size without significantly altering synthesis kinetics. Thus, combining the two pore expanders in the order first TMB and second decane, enhances pore expansion more effectively than using a single agent. Thus, to ensure proper pore expansion without disordering or damaging the mSiO_2 structure, a balanced combination of decane and a lower concentration of TMB was used, effectively aligning pore expansion rates with the mSiO_2 formation process.

UV-Vis, XPS and DLS (Figure 2f–h) characterization of the selected CeO_2@mSiO_2 ($D_P \approx 11$ nm) further validated the core-shell properties and the maintenance of the CeO_2 cores physicochemical characteristics in the core-shell structure. The UV spectrum displayed the characteristic Ce^{4+} absorption peak at 294 nm, confirming the successful incorporation of CeO_2 NZs into the mesoporous silica. XPS analysis revealed a mixed valence state of Ce, with Ce^{4+} and Ce^{3+} ratios of approximately 70.9% and 29.1%, respectively, similar as the pre-synthesized CeO_2 cores, indicating that the sol–gel synthesis method preserves the valence state of Ce, thereby maintaining the catalytic activity of the CeO_2 NZs within the composite.

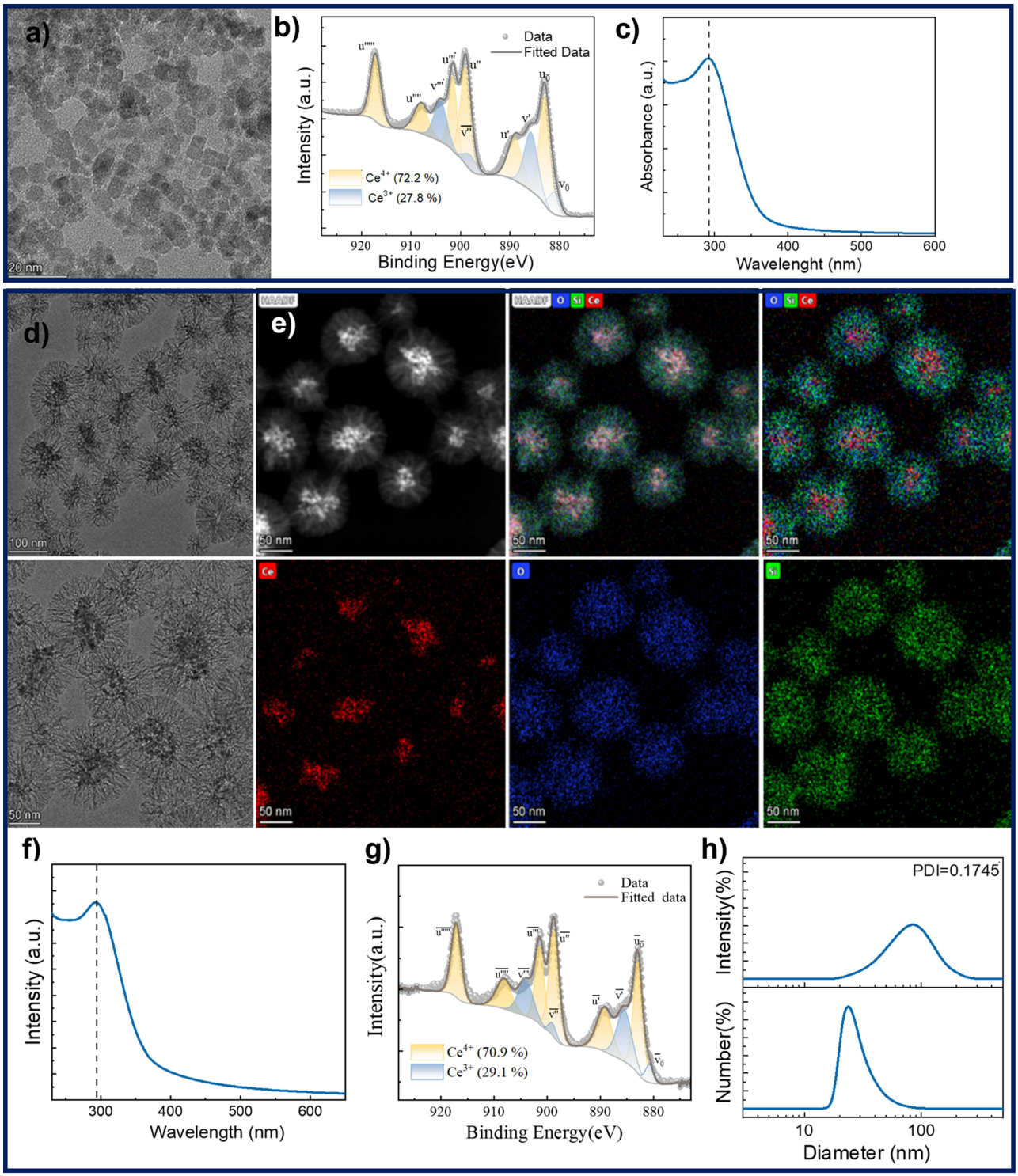

Figure 2 Characterization of the CeO_2 cores and CeO_2@$mSiO_2$ sample. (**a–c**) TEM image, XPS and UV-VIS, respectively, of the CeO_2 cores. (**d**) TEM images at different magnifications of the CeO_2@$mSiO_2$. (**e**) High-angle annular dark-field (HAADF) images of the CeO_2@$mSiO_2$ and the elemental mapping of Ce, O, Si, and overlapping of these elements. (**f** and **g**) UV-VIS and XPS respectively of the CeO_2@$mSiO_2$, where it can be observed the maintenance of the physicochemical characteristics of the CeO_2 cores inside the $mSiO_2$ shell. (**h**) DLS measurements of the hydrodynamic diameter (D_H) by intensity distribution (top) and number distribution (bottom) of the CeO_2@$mSiO_2$. This characterization corresponds to the sample with ($D_P \approx 11$ nm).

https://doi.org/10.2147/IJN.S525411

Table 1 Synthesis Parameters for the Obtention of CeO_2@$mSiO_2$ Samples with Different D_P

Sample	v(EtOH) /v(H_2O)	Decane:TMB (mol ratio)	n(TEOS)/ n(CTAB)	Stirring time (min)		CTAB removal
				Decane	TMB	
D_P = 3.65 nm	2:8	0	3.30	30	90	NH_4NO_3 in ethanol
D_P = 6.15 nm	2.27:7.73	10:2	3.85	90	120	NH_4NO_3 in ethanol
D_P = 11.03 nm	2.27:7.73	10:2	3.85	90	120	Saturated NaCl in methanol

To evaluate the pore size distribution of CeO_2@$mSiO_2$ after CTAB removal, N_2 adsorption-desorption analysis was performed using a fully automated specific surface and porosity analyzer (Figure 3). The specific surface area was calculated using the BET method, and the pore size distribution was determined via density functional theory (DFT). For CeO_2@$mSiO_2$ nanocomposites synthesized without pore expanders, a pore size of 3.65 nm was obtained (Figure 3a). In contrast, CeO_2@$mSiO_2$ synthesized with pore expanders and treated with NH_4NO_3 for surfactant removal exhibited a larger pore size of 6.15 nm, approximately twice the original size (Figure 3b). Conversely, using saturated NaCl in methanol for CTAB removal, the largest pore size (11.03 nm) was achieved (Figure 3c). This enhanced efficiency in expanding the pores is likely due to the higher ionic strength provided by the greater solubility in methanol of NaCl, which facilitates more effective CTAB removal. It can be observed that the increase in pore size is accompanied by a decrease in the specific surface area of CeO_2@$mSiO_2$, attributed to the thinning of pore walls, which reduces the effective surface area per unit volume. These results confirm the successful synthesis of nanocomposites with enlarged pores using an improved sol–gel method.

Loading and Release Studies of Que Into CeO_2@$mSiO_2$ Core-Shell Nanoparticles

As known, the loading capacity of drugs into $mSiO_2$ depends on factors like the affinity of the drug for the silica substrate, the silica pore volume, and the drug concentration in the solution. The choice of drug loading method also influences the loading

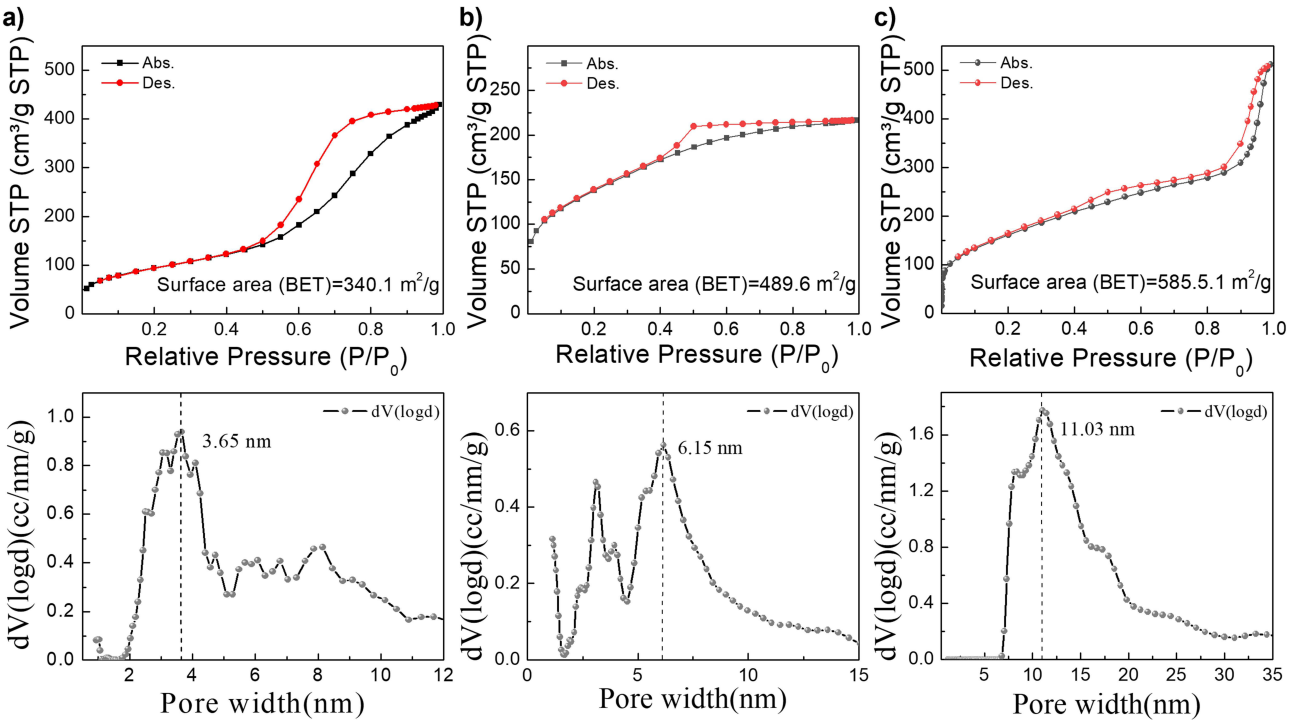

Figure 3 Adsorption-desorption isotherms (left column) and DFT pore size distribution (right column of the different CeO_2@$mSiO_2$ samples. (**a**) CeO_2@$mSiO_2$ with D_P = 3.65 nm. (**b**) CeO_2@$mSiO_2$ with D_P = 6.15 and employing NH_4NO_3 for CTAB removal. (**c**) CeO_2@$mSiO_2$ with D_P = 11.03 nm and employing using saturated NaCl in methanol for CTAB removal.

amount, drug distribution, and the physicochemical properties of the drug within the mesoporous structure. Common drug loading methods include melting, solvent impregnation, incipient wetness impregnation, supercritical fluid technology, and co-spray drying, with solvent impregnation being the most widely used.[53,54] In the case of Que, it is poorly soluble in hydrophilic solvents and contains hydroxyl groups that readily form hydrogen bonds with the silanol groups of the $mSiO_2$. Thus, solvent impregnation was chosen in this work to load quercetin to obtain the $(CeO_2/Que)@mSiO_2$ nanocomposites.

To determine the optimal drug loading conditions, several factors were considered. First, the molecular size of Que was calculated according to Density Functional Theory. Chem3D software was used to construct a three-dimensional spatial model of the Que molecule, and the size of Que was calculated by using the van der Waals radius.[55] The results showed that the molecular size of Que was ≥1.3 nm, and it could be loaded into $mSiO_2$ with a pore size greater than 4 nm. This suggests that Que should be loaded into $mSiO_2$ with pore sizes between 5 and 15 nm to avoid low loading efficiency in smaller pores and rapid drug release from larger pores. Additionally, at high loading amounts (>10%), Que may recrystallize within the pores, causing blockages.[54]

UV-Vis spectrophotometry was used to measure the drug loading efficiency of Que in $CeO_2@mSiO_2$ (Figure 4). For this study, the drug loading capacities of $CeO_2@mSiO_2$ with pore diameters of approximately 3 nm, 6 nm, and 11 nm were compared. $CeO_2@mSiO_2$ (D_P≈3 nm) and $CeO_2@mSiO_2$ (D_P≈6 nm) were prepared by removing CTAB using an

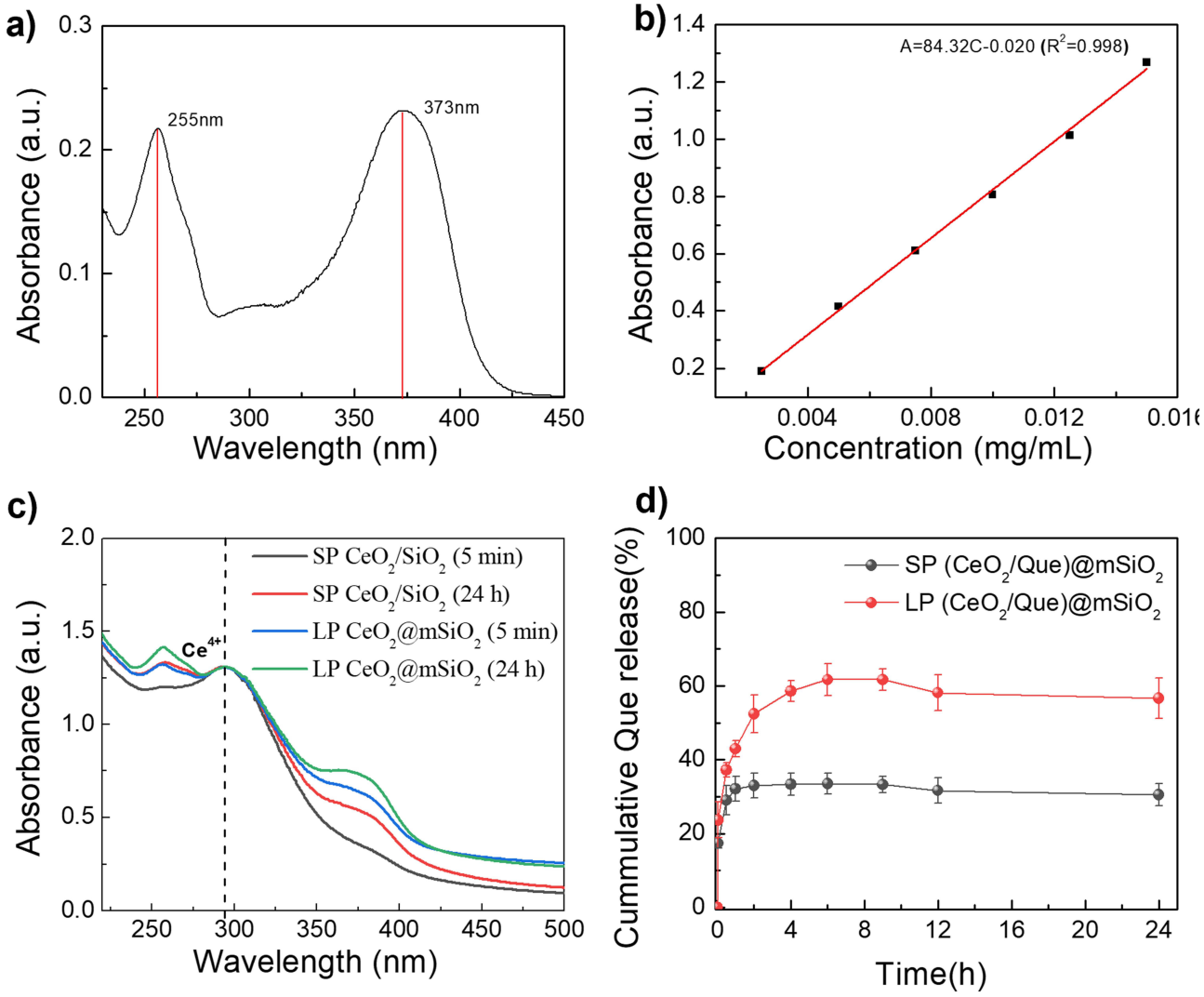

Figure 4 Loading and release studies of Que in the $CeO_2@mSiO_2$. (**a**) UV-Vis spectrum of Que. (**b**) Calibration curve of Que in anhydrous ethanol. (**c**) UV-Vis spectroscopy of Small Pore (SP) $CeO_2@mSiO_2$ (D_P ≈ 3 nm) and large pore (LP) $CeO_2@mSiO_2$ (D_P ≈ 11 nm) loaded with Que 5 minutes and 24 hours after impregnation. (**d**) Cumulative release of Que from the same nanocomposites in PBS buffer (pH=7.4).

https://doi.org/10.2147/IJN.S525411

NH_4NO_3 buffer, while CeO_2@$mSiO_2$ (D_P≈11 nm) was also prepared by removing CTAB with saturated NaCl in methanol. The results showed that, as expected, CeO_2@$mSiO_2$ (D_P≈6 nm) achieved a 35.6% higher drug loading capacity compared to CeO_2@$mSiO_2$ (D_P≈3 nm) and CeO_2@$mSiO_2$ (D_P≈11 nm) exhibited the highest drug loading capacity, approximately twice that of CeO_2@$mSiO_2$ (D_P≈3 nm). In detail, from a saturated Que solution in ethanol (14.89 mg/mL) and at a drug loading ratio of 1:1 (m_{Que}:$m_{CeO2@mSiO2}$), 2.5 ± 0.1% was loaded in CeO_2@$mSiO_2$ (D_P≈3 nm), 3.4 ± 0.05% in CeO_2@$mSiO_2$ (D_P≈6 nm) and 4.8 ± 0.1% in CeO_2@$mSiO_2$ (D_P≈11 nm).

Additionally, the loading process was faster for CeO_2@$mSiO_2$ with larger pores indicating that a larger pore size allows for more efficient and rapid adsorption of Que using the solvent impregnation method. In detail, after mixing the saturated ethanol solution of Que with CeO_2@$mSiO_2$ (D_P≈11 nm) for 5 minutes, the amount of loaded Que was already higher than in CeO_2@$mSiO_2$ after 24 hours.

As the initial drug loading efficiency was relatively low compared to existing studies of loading natural products in $mSiO_2$, the drug loading ratios were adjusted to optimize the process. The mass ratios of Que to CeO_2@$mSiO_2$ (m_{Que} :$m_{CeO_2@mSiO_2}$) were tested at 3:1, 2:1, 1:1, 1:2, and 1:3. Table 2 presents the drug loading efficiency and amounts for each ratio. The results demonstrate that a 3:1 mass ratio achieved the highest drug loading efficiency (c.a. 15%), which was employed for further experiments.

To evaluate the drug release behavior of (CeO_2/Que)@$mSiO_2$ in HEPES buffer and compare the effects of different pore sizes on drug release, an in vitro release experiment was conducted using (CeO_2/Que)@$mSiO_2$ (D_P≈11 nm) prepared at loading rations 3:1 as described above, which was compared with (CeO_2/Que)@$mSiO_2$ (D_P≈ 3 nm). The in vitro cumulative release curve of Que. (CeO_2/Que)@$mSiO_2$ (D_P≈11 nm) exhibited a cumulative release rate of nearly 60% within 24 hours, with a burst release occurring during the first 3 hours. In contrast, (CeO_2/Que)@$mSiO_2$ (D_P≈ 3 nm) achieved a cumulative release rate of 33%, approximately half that of (CeO_2/Que)@$mSiO_2$ (D_P≈ 11 nm). This indicates that enlarging the pore size not only increases the drug loading capacity but also provides better control over the release rate, maintaining a higher drug concentration for a longer period within 24 hours.

Characterization of the (CeO_2/Que)@$mSiO_2$ Nanocomposites

The (CeO_2/Que)@$mSiO_2$ (D_P≈11 nm) nanocomposite was selected for further experiments and characterized using UV-Vis, FT-IR, and XRD techniques (Figure 5). The UV-Vis spectrum (Figure 5a) of (CeO_2/Que)@$mSiO_2$ shows both the characteristic absorption peak of Ce^{4+} from the CeO_2 cores and the absorption peak of Que, indicating the successful formation of the composite. The FT-IR spectrum shown in Figure 5b reveals the different characteristic CeO_2 and Que absorption peaks. The band at 556 cm^{-1} corresponds to the Ce-O stretching vibration of CeO_2, while the absorption band at 1660 cm^{-1} is assigned to the stretching vibration of the carbonyl group (C=O) in Que.[56,57] The intense peak at 1093 cm^{-1} reflects the Si-O antisymmetric stretching vibration in $mSiO_2$, with additional Si–O bands appearing at 799 cm^{-1} (symmetric stretching) and 470 cm^{-1} (bending), consistent with the silica framework. Furthermore, the stretching vibrations of hydroxyl groups (OH) in CeO_2@$mSiO_2$ and (CeO_2/Que)@$mSiO_2$ appear at 3373 cm^{-1}, 3421 cm^{-1}, and 3439 cm^{-1}, respectively.[56,57]

Of particular note is the evolution of the O–H stretching region. The broad bands at 3373 cm^{-1} (CeO_2@$mSiO_2$), 3421 cm^{-1}, and 3439 cm^{-1} ((CeO_2/Que)@$mSiO_2$) show a progressive red shift and increased asymmetry upon Que incorporation. This broadening and shift suggest hydrogen bonding interactions between Que hydroxyl groups and the

Table 2 Que Loading Ratios (m_{Que} :$m_{CeO2@mSiO_2}$) and Loading Efficiency

Loading Ratio	Loading Efficiency (%)
3:1	15.67
2:1	8.79
1:1	4.8
1:2	2.28
1:3	1.94

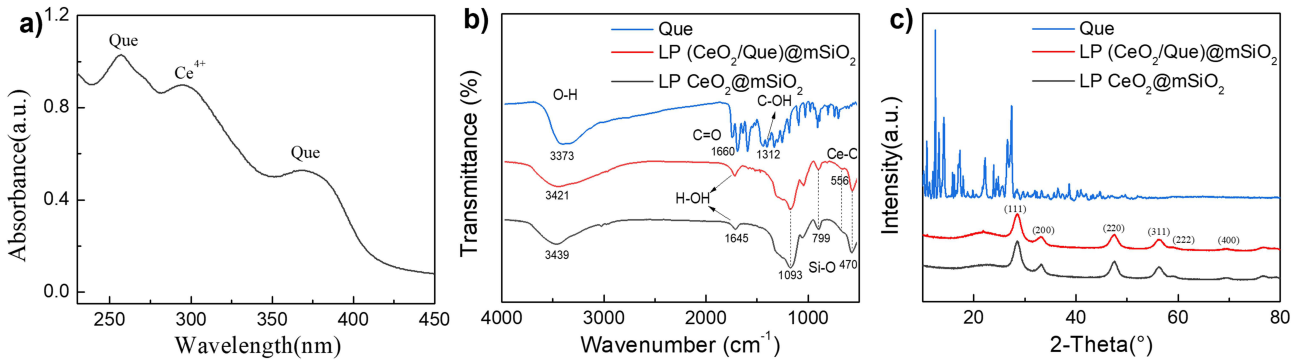

Figure 5 Characterization of the $(CeO_2/Que)@mSiO_2$ nanocomposites. (**a**) UV-VIS spectrum with the characteristic Ce^{4+} and Que peaks. (**b**) FTIR spectrum of Que, large pore (LP) $CeO_2@mSiO_2$ core-shell structure and LP $(CeO_2/Que)@mSiO_2$ nanocomposites. (**c**) Corresponding XRD diffraction pattern.

silanol groups on the silica surface. Although the distinct Que absorption bands are less intense in the composite spectrum, this likely reflects strong interactions between Que and the porous matrix, leading to its predominant amorphous state and reduced vibrational freedom. These observations confirm the successful loading and intimate integration of Que within the $mSiO_2$ structure, further supporting the composite's stability and potential for sustained release.

To further evaluate the structure of the $(CeO_2/Que)@mSiO_2$ nanocomposites, XRD analysis was performed (Figure 5c). The XRD pattern of $(CeO_2/Que)@mSiO_2$ exhibits diffraction peaks corresponding to the characteristic crystal planes of CeO_2NZs, specifically at the (111), (200), (220), (220), (311), and (400) planes. These diffraction peaks match those of $CeO_2@mSiO_2$, confirming the presence of the CeO_2 cores in the composite material. However, the XRD pattern does not show any diffraction peaks for crystalline Que. Similar to FTIR results, this also suggests that Que is likely incorporated into the $mSiO_2$ in its amorphous state, indicating that Que interacts with the $mSiO_2$ surface most likely forming intermolecular hydrogen bonds with the silanol groups of silica.[58]

Cell Viability and ROS Scavenging Activity of $(CeO_2/Que)@mSiO_2$ Nanocomposites

To evaluate the effect of $(CeO_2/Que)@mSiO_2$ on cell viability, an MTT assay was conducted using A549 human cells at concentrations ranging from 1.56 to 100 μg/mL for CeO_2NZs and 15 μg/mL of Que maintained for all experiments. The results showed that cells treated with $(CeO_2/Que)@mSiO_2$ exhibited viability comparable to the control across a wider range of concentrations than those treated with free Que (Figure 6a). These findings align with previous studies on Que[59] and similar non-Que-loaded $CeO_2@mSiO_2$ nanocomposites[51] and suggest that incorporating CeO_2 and Que into the nanocomposite may enhance its biocompatibility while reducing the toxicity associated with Que alone. This combination not only maintains cellular viability but may also improve the therapeutic index by enabling a wider dosing window compared to free Que.

Next, to initially assess the antioxidant potential of these materials, cells were preincubated with H_2O_2 for 45 minutes. Following this, Que, $CeO_2@mSiO_2$, and $(CeO_2/Que)@mSiO_2$ were added, and cell viability was assessed after 24 hours. As expected, H_2O_2 treatment significantly reduced cell viability to 35.44%, whereas the addition of all materials improved cell viability, with the highest increase observed for $(CeO_2/Que)@mSiO_2$, reaching up to 53.88% (Figure 6b), being a 52.1% increase in cell viability compared to H_2O_2-treated cells.

The ROS levels in A549 cells were measured by flow cytometry and inverted fluorescence microscopy to evaluate the ROS scavenging ability of the $(CeO_2/Que)@mSiO_2$ nanocomposites. To establish an oxidative stress model, the study first assessed the ROS levels induced by different concentrations of H_2O_2 at various exposure times, which indicated that a 45-minute exposure to 10 mM H_2O_2 was optimal for inducing oxidative stress (Supporting Information, Figure S1). Figure 6c shows the ROS flow cytometry analysis for Que, $CeO_2@mSiO_2$, and $(CeO_2/Que)@mSiO_2$ after inducing oxidative stress in A549 cells with H_2O_2 for 45 minutes. Following H_2O_2 exposure, the ROS fluorescence intensity was 33%, compared to less than 1% in the control group (no H2O2), confirming the successful induction of a significant cellular oxidative stress. When comparing the ROS scavenging abilities of Que (15 and 30 μg/mL), $CeO_2@mSiO_2$ (15 and 30 μg/mL of CeO_2 content), and $(CeO_2/Que)@mSiO_2$ (both loaded at 15 and 30 μg/mL), $(CeO_2/Que)@mSiO_2$

https://doi.org/10.2147/IJN.S525411

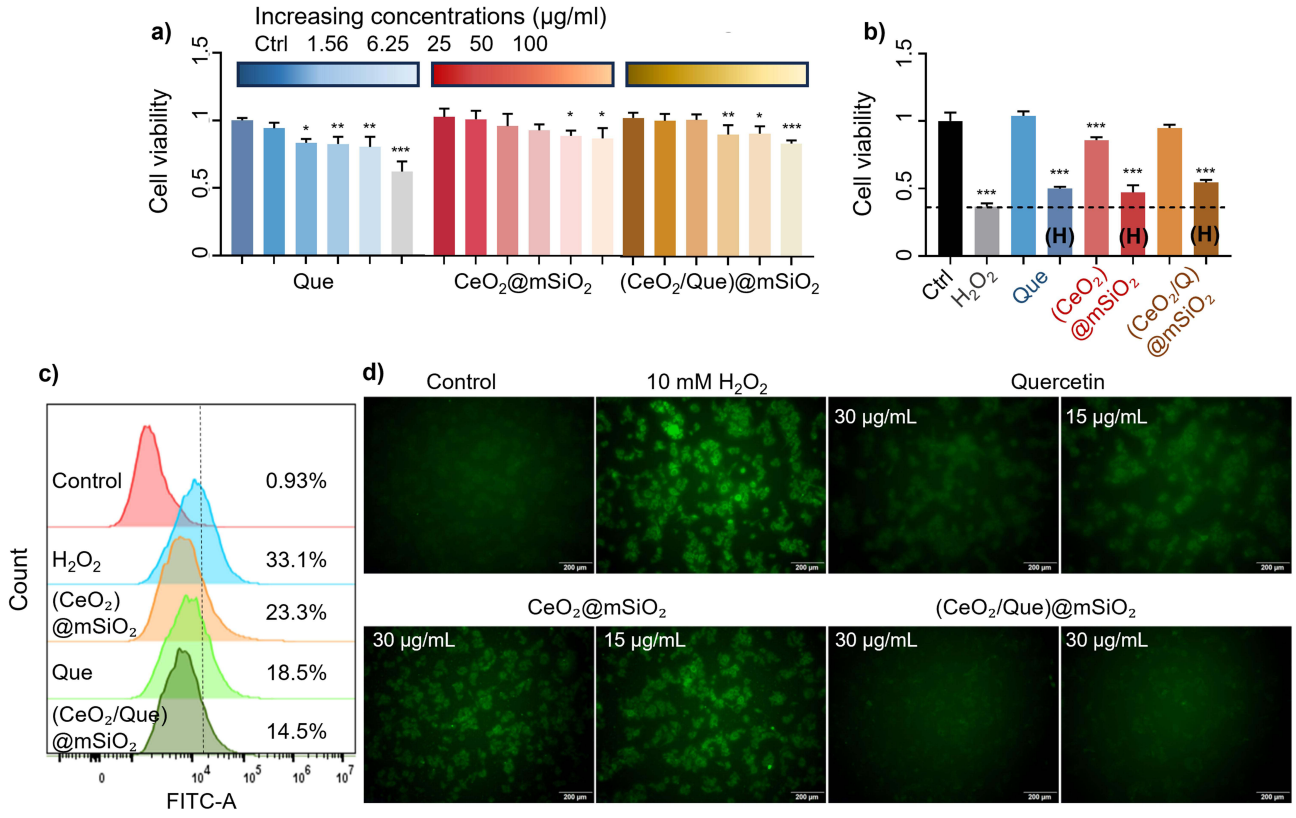

Figure 6 In vitro evaluation of cell viability and ROS-scavenging effects of the $(CeO_2/Que)@mSiO_2$ in A59 cells. (**a**) Cell viability of A549 cells exposed to Que, CeO_2 $@mSiO_2$, and $(CeO_2/Que)@mSiO_2$ (n=3, *p<0.05 vs control, **p<0.01, ***p<0.001). (**b**) Cell viability of A549 cells exposed to the same materials pre-incubated with 10 mM of H_2O_2 for 45 minutes (denoted with (H)) and not pre-incubated (*p<0.05 vs control, **p<0.01, ***p<0.001). (**c**) Flow cytometric analysis of reactive oxygen species (ROS) generation using DCFH-DA fluoroprobe in A549 cells. (**d**) Representative images of the flow cytometry quantitation. Decreased diffused green fluorescence is visible in all cases compared with cells treated with H_2O_2.

exhibited the highest ROS scavenging capacity. Figure 6d presents the corresponding representative images of the flow cytometry quantitation of Que, $CeO_2@mSiO_2$, and $(CeO_2/Que)@mSiO_2$ in scavenging ROS produced by A549 cells exposed to H_2O_2. Overall, the results suggest that the combination of Que and CeO_2 in the same nanocomposite offers enhanced cellular protection against oxidative stress.

Analysis of Inflammatory Genes Expression in Response to Oxidative Stress

To evaluate the potential of $(CeO_2/Que)@mSiO_2$ in mitigating inflammatory responses, the expression levels of inflammatory genes were measured, with ROS levels serving as indicators of oxidative stress-induced inflammation. The optimal conditions for an inflammatory cell model were determined (Figures S2 and S3). It was observed that the expression of the proinflammatory factor genes Tnfα, IL1β and IL6 progressively increased over a 3-hour period, and exposure to 500 μM H_2O_2 for 3 hours was identified as the optimal condition for simulating an inflammatory cell state without inducing significant cytotoxicity.

Next, the effect of the $(CeO_2/Que)@mSiO_2$ nanocomposite on the gene expression of pro-inflammatory markers was evaluated. The results showed that the combination of Que with CeO_2 significantly downregulated IL1β, IL6 and TNFα (Figure 7). This effect was not observed with free Que which did not lead to a significant down-regulation of these inflammatory genes at the same concentration. This indicates that the dual presence of CeO_2 and Que within the same nanocomposite also enhances the anti-inflammatory response. In summary, the findings demonstrate a positive and improved impact of the $(CeO_2/Que)@mSiO_2$ on cell viability, oxidative stress, and cellular inflammation.

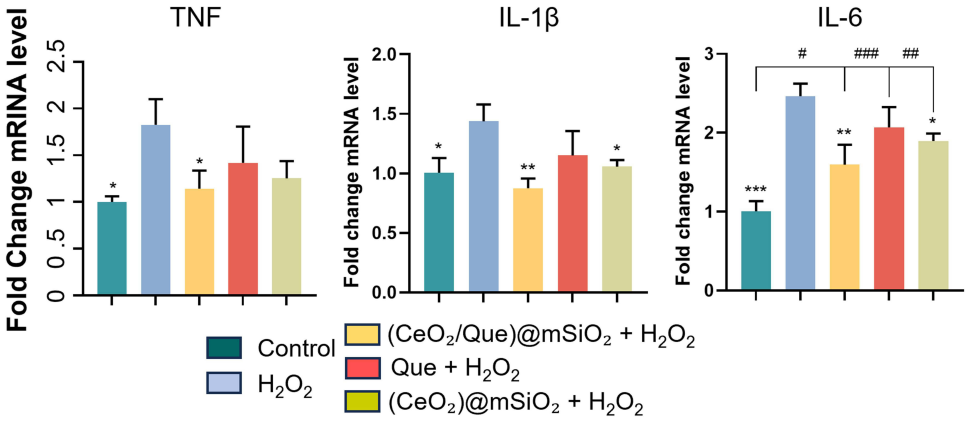

Figure 7 Inflammatory genes expression. Relative expression levels of TNF-α, IL-1β and IL-6 mRNA from A549 cells exposed to Que, CeO_2@$mSiO_2$, and (CeO_2/Que)@$mSiO_2$ (n=3, *p<0.05 vs H_2O_2, **p<0.01, ***p<0.001; #p< 0.05 vs control, ##p<0.01, ###p<0.001).

Discussion

The integration of natural antioxidants with synthetic NZs represents a promising approach to overcoming the limitations of conventional antioxidant therapies and, specifically, there have been previous assessments of the synergistic effects of Que and CeO_2NPs in some therapeutic contexts. In periodontal disease models, Que-functionalized nano-octahedral ceria synergistically modulated immunity by increasing the M2/M1 macrophage polarization ratio and regulating cytokine expression.[60] Also, Que immobilized on nanoceria was shown to ameliorate glutamate-induced neurotoxicity in neurons.[61] Additionally, complexes of Que and curcumin with cerium ions demonstrated reduced toxicity in photodynamic treatments of breast and melanoma cancer cells compared to each compound alone.[49] Moreover, hollow mesoporous CeO_2NPs loaded with Que effectively inhibited inflammation by suppressing M1 macrophage polarization in mouse models of flap surgery.[50]

In this study, we developed a core-shell nanocomposite (CeO_2/Que)@$mSiO_2$, which combines the potent antioxidant and anti-inflammatory properties of Que with the multi-enzymatic and ROS-scavenging capabilities of CeO_2NZs. The nanocarrier $mSiO_2$ have been widely explored due to their structural robustness, tunable pore size, high surface area, and biocompatibility, making them ideal candidates for the delivery of poorly soluble drugs. Importantly, $mSiO_2$ have been classified as GRAS (Generally Recognized As Safe) by the FDA, highlighting their biocompatibility and biodegradability, which makes it suitable for drug delivery applications via different administration routes.[62] The selected NZs for this study, CeO_2NZs are among the most versatile and effective NZs, recognized for over two decades[63] for their multienzymatic activities and ability to modulate cellular microenvironments.[40,64] These nanoparticles mimic the functions of natural enzymes such as catalase (CAT),[43,44] superoxide dismutase (SOD),[41,65] and peroxidase e, enabling the neutralization of reactive oxygen species (ROS) through multiple pathways. CeO_2NZs are distinguished by their unique redox-switching between Ce^{3+} and Ce^{4+} oxidation states, facilitating continuous regeneration and sustained ROS scavenging.[40]

Furthermore, CeO_2NZs exert anti-inflammatory effects by modulating inflammatory signaling pathways and have been explored in different medical fields, including cardiology, hepatology, nephrology, neurodegenerative diseases, skin regeneration and wound healing.[66–68] For example, Sener et al developed a biomaterial system for delivering CeO_2NZs loaded with microRNA-146a to diabetic wounds, demonstrating high in vivo efficacy in a diabetic mouse wound healing model.[69] All these properties make CeO_2NZs a powerful complement to Que, offering a synergistic strategy to combat oxidative stress and inflammation effectively.

Our characterization studies confirmed the successful integration of CeO_2NZs within the $mSiO_2$ structure, which allows to maintain their physicochemical and catalytic properties.[34] The synthesis of these nanocomposites was optimized using a sol–gel method with pore-expanding strategies, leading to an enhanced drug loading efficiency and controlled release of Que in biological environments, as showed in previous studies with single-component systems.[34,70] Biological evaluations demonstrated that (CeO_2/Que)@$mSiO_2$ do not compromise cell viability within a concentration ranges that show antioxidant and anti-inflammatory effects (1.56–100 μg/mL for CeO) NZs and 15 μg/mL for Que A549 cells. The incorporation of Que into the composite exhibited a synergistic effect, combining the sustained catalytic

https://doi.org/10.2147/IJN.S525411

activity of CeO_2NZs with the potent, albeit transient, antioxidant properties of Que. In addition to its antioxidant capacity, Que has been extensively studied for its anti-inflammatory effects, which include downregulation of proinflammatory cytokines such as TNF-α, IL-1β, and IL-6.[5]

The results of this study further support the role of Que in inflammation modulation, as cells treated with (CeO_2/Que)@$mSiO_2$ exhibited lower expression levels of these inflammatory markers compared to untreated cells. Notably, the composite demonstrated a greater reduction in IL-1β and IL-6 expression compared to free Que, suggesting that the NZ component contributes to a prolonged anti-inflammatory effect. This is important since chronic inflammation is a major contributor to many diseases and oxidative stress-related disorders, highlighting the need for advanced therapeutic strategies for effective management. Thus, overall, this study highlights the potential of combining natural antioxidants with synthetic NZs providing a multifunctional therapeutic nanoplatform (CeO_2/Que)@$mSiO_2$) to effectively address oxidative stress and inflammation. The findings provide valuable insights into the design of advanced drug delivery systems and can also be extended to the development of nanoparticle-based dressings and bioengineered materials incorporating antioxidants and NZ agents to accelerate tissue repair and reduce oxidative damage.[47,69]

Despite these promising findings, some limitations must be considered. The delayed release kinetics of Que within the nanocomposite may affect its bioavailability at specific therapeutic windows, indicating further optimization of loading concentrations and release profiles depending on the clinical application. Additionally, while CeO_2 NZs have demonstrated excellent biocompatibility in various studies, their long-term interactions within biological systems require further investigation to ensure safety and minimize potential cytotoxic effects.[40] Future studies should explore in vivo models to assess the pharmacokinetics, biodistribution, and therapeutic efficacy of (CeO_2/Que)@$mSiO_2$ in relevant disease contexts, such as chronic inflammation and oxidative stress-related disorders.

Additionally, this study focused on evaluating the nanocomposite's behavior under physiological conditions, it does not assess the pH-dependent release behavior of the system. This formulation is intended for applications in environments with near-neutral pH, such as chronic inflammatory tissues. However, for potential applications in more acidic pathological environments (eg, tumor microenvironments or infected tissues), future studies are needed to explore stimulus-responsive behavior at varying pH levels. Such investigations would help to further tailor the nanoplatform for site-specific or condition-responsive drug delivery.

Conclusions

This study presents a novel nanocomposite, (CeO_2/Que)@$mSiO_2$, that integrates the advantages of synthetic NZs and natural antioxidants to enhance therapeutic efficacy against oxidative stress and inflammation. The results demonstrate that the $mSiO_2$ shell significantly improves Que loading and release, while the incorporation of CeO_2NZs provides sustained ROS-scavenging activity. Biological evaluations confirm the biocompatibility and synergistic antioxidative and anti-inflammatory effects of the composite, highlighting its potential for biomedical applications such as the incorporation in dressing for wound ulcerations. However, metallic and metal oxide nanoparticles, often used in NZs design, may themselves trigger inflammatory responses depending on factors such as size, surface chemistry, and immune interactions (TOOBA2024). Understanding these mechanisms is critical to engineering safer and more effective nanozyme-based therapies. Future investigations should focus on optimizing release kinetics and evaluating in vivo efficacy to facilitate clinical translation.

Acknowledgments

This work was supported by grants from the Research Funding for Doctoral Talents of the First Affiliated Hospital of Anhui Medical University (grant No.1952); the Instituto de Salud Carlos III (PI24/00688 and BA22/00017 to G. C.), co-financed by FEDER, European Union, "A way of making Europe"; Agencia Estatal de Investigación (Project PID2022-138243OB-I00 funded by MICIU/AEI /10.13039/501100011033 and by FEDER, UE, to M.M.-R.). Consolidated Research Group, Departament de Recerca i Universitats de la Generalitat de Catalunya (2021 SGR 00881 to M.M.-R.). CIBERehd is financed by the Instituto de Salud Carlos III.

Author Contributions

All authors made a significant contribution to the work reported, whether that is in the conception, study design, execution, acquisition of data, analysis and interpretation, or in all these areas; took part in drafting, revising or critically reviewing the article; gave final approval of the version to be published; have agreed on the journal to which the article has been submitted; and agree to be accountable for all aspects of the work.

Disclosure

The authors report no conflicts of interest in this work.

References

1. Chen X, Yin OQP, Zuo Z, et al. Pharmacokinetics and modeling of quercetin and metabolites. *Pharm Res*. 2005;22(6):892–901. doi:10.1007/s11095-005-4584-1
2. Luo M, Tian R, Yang Z, et al. Quercetin suppressed NADPH oxidase-derived oxidative stress via heme o xygenase-1 induction in macrophages. *Arch Biochem Biophys*. 2019;671:69–76. doi:10.1016/j.abb.2019.06.007
3. Salehi B, Machin L, Monzote L, et al. Therapeutic potential of quercetin: new insights and perspectives for human health. *ACS Omega*. 2020;5(20):11849–11872. doi:10.1021/acsomega.0c01818
4. Shen P, Lin, W, Deng, X, et al. Potential implications of quercetin in autoimmune diseases. *Front Immunol*. 2021;12.
5. Wang G, Wang Y, Yao L, et al. Pharmacological activity of quercetin: an updated review. *Evid Based Complement Alternat Med*. 2022;2022(1):3997190. doi:10.1155/2022/3997190
6. Sul O-J, Ra S-W. Quercetin prevents LPS-induced oxidative stress and inflammation by modulating NOX2/ROS/NF-kB in lung epithelial cells. *Molecules*. 2021;26:6949. doi:10.3390/molecules26226949
7. Xu D, Hu, MJ, Wang, YQ, et al. Antioxidant activities of quercetin and its complexes for medicinal application. *Molecules*. 2019;24(6).
8. Zhang Y, Wang H, Yang R, et al. Synergistic therapeutic effects of D-Mannitol–Cerium–Quercetin (Rutin) coordination polymer nanoparticles on acute lung injury. *Molecules*. 2024;29(12):2819. doi:10.3390/molecules29122819
9. Zhang Y-M, Zhang Z-Y, Wang R-X. Protective mechanisms of quercetin against myocardial ischemia reperfusion injury. *Front Physiol*. 2020;11:11. doi:10.3389/fphys.2020.00011
10. Kandemir K, Tomas, M, McClements, DJ, et al. Recent advances on the improvement of quercetin bioavailability. *Trends Food Sci Technol*. 2021;119.
11. Tomou EM, Papakyriakopoulou P, Saitani E-M, et al. Recent advances in nanoformulations for quercetin delivery. *Pharmaceutics*. 2023;15(6):1656. doi:10.3390/pharmaceutics15061656
12. Almeida AF, Borge GIA, Piskula M, et al. Bioavailability of quercetin in humans with a focus on interindividual variation. *Compr Rev Food Sci Food Saf*. 2018;17(3):714–731. doi:10.1111/1541-4337.12342
13. Graefe EU, Derendorf H, Veit M. Pharmacokinetics and bioavailability of the flavonol quercetin in humans. *Int J Clin Pharmacol Ther*. 1999;37(5):219–233.
14. Khursheed R, Singh SK, Wadhwa S, et al. Enhancing the potential preclinical and clinical benefits of quercetin through novel drug delivery systems. *Drug Discovery Today*. 2020;25(1):209–222. doi:10.1016/j.drudis.2019.11.001
15. Riva A, Ronchi M, Petrangolini G, et al. Improved oral absorption of quercetin from quercetin Phytosome®, a new delivery system based on food grade lecithin. *Eur J Drug Metabol Pharmacokin*. 2019;44(2):169–177. doi:10.1007/s13318-018-0517-3
16. Srisa-nga K, Mankhetkorn S, Okonogi S, et al. Delivery of superparamagnetic polymeric micelles loaded with quercetin to hepatocellular carcinoma cells. *J Pharmaceut Sci*. 2019;108(2):996–1006. doi:10.1016/j.xphs.2018.08.008
17. Catauro M, Papale F, Bollino F, et al. Silica/quercetin sol-gel hybrids as antioxidant dental implant materials. *Sci Technol Adv Mater*. 2015;16(3):035001. doi:10.1088/1468-6996/16/3/035001
18. Nday CM, Halevas E, Jackson GE, et al. Quercetin encapsulation in modified silica nanoparticles: potential us e against Cu(II)-induced oxidative stress in neurodegeneration. *J Inorganic Biochem*. 2015;145:51–64. doi:10.1016/j.jinorgbio.2015.01.001
19. Ugazio E, Gastaldi L, Oliaro-Bosso S. Thermoresponsive mesoporous silica nanoparticles as a carrier for skin delivery of quercetin. *Int J Pharm*. 2016;511(1):446–454. doi:10.1016/j.ijpharm.2016.07.024
20. Caddeo C, Pons R, Carbone C, et al. Physico-chemical characterization of succinyl chitosan-stabilized lipo somes for the oral co-delivery of quercetin and resveratrol. *Carbohydr Polym*. 2017;157:1853–1861. doi:10.1016/j.carbpol.2016.11.072
21. Rezaei-Sadabady R, Eidi, A, Zarghami, N, et al. Intracellular ROS protection efficiency and free radical-scavenging ac tivity of quercetin and quercetin-encapsulated liposomes. *Artificial Cells Nanomed Biotechnol*. 2016;44(1):128–134.
22. Sun J, Li M, Lin K, et al. Delivery of quercetin for breast cancer and targeting potentiation via hyaluronic nano-micelles. *Int J Biol Macromol*. 2023;242:124736. doi:10.1016/j.ijbiomac.2023.124736
23. Ferrentino N, Romano MP, Zappavigna S, et al. Poly(ε-caprolactone)-poly(ethylene glycol) tri-block copolymer as quercetin delivery system for human colorectal carcinoma cells: synthesis, characterization and in vitro study. *Polymers*. 2023;15(5):1179. doi:10.3390/polym15051179
24. Caro C, Pourmadadi M, Eshaghi MM, et al. Nanomaterials loaded with quercetin as an advanced tool for cancer treatment. *J Drug Delivery Sci Technol*. 2022;78:103938. doi:10.1016/j.jddst.2022.103938
25. Kandemir K, Tomas M, McClements DJ, et al. Recent advances on the improvement of quercetin bioavailability. *Trends Food Sci Technol*. 2022;119:192–200. doi:10.1016/j.tifs.2021.11.032
26. Boots AW, Drent M, de Boer VCJ, et al. Quercetin reduces markers of oxidative stress and inflammation in sarcoidosis. *Clin Nutr*. 2011;30(4):506–512. doi:10.1016/j.clnu.2011.01.010
27. Costa LG, Garrick JM, Roquè PJ, et al. Mechanisms of neuroprotection by quercetin: counteracting oxidative stress and more. *Oxid Med Cell Longev*. 2016;2016(1):2986796. doi:10.1155/2016/2986796

28. Dai C, Sharma G, Liu G, et al. Therapeutic detoxification of quercetin for aflatoxin B1-related toxicity: roles of oxidative stress, inflammation, and metabolic enzymes. *Environ Pollut*. 2024;345:123474. doi:10.1016/j.envpol.2024.123474
29. Li F, Liu, J, Tang, S, et al. Quercetin regulates inflammation, oxidative stress, apoptosis, and mitochondrial structure and function in H9C2 cells by promoting PVT1 expression. *Acta Histochem*. 2021;123(8):151819.
30. Liu Z, Ren Z, Zhang J, et al. Role of ROS and nutritional antioxidants in human diseases. *Front Physiol*. 2018;9. doi:10.3389/fphys.2018.00477
31. Oboh G, Ademosun AO, Ogunsuyi OB. Quercetin and its role in chronic diseases. In: Gupta SC, Prasad S, Aggarwal BB, editors. *Drug Discovery From Mother Nature*. Cham: Springer International Publishing; 2016:377–387.
32. Zhou Y, Qian C, Tang Y, et al. Advance in the pharmacological effects of quercetin in modulating oxidative stress and inflammation related disorders. *Phytother Res*. 2023;37(11):4999–5016. doi:10.1002/ptr.7966
33. Slika H, Mansour H, Wehbe N, et al. Therapeutic potential of flavonoids in cancer: ROS-mediated mechanisms. *Biomed Pharmacother*. 2022;146:112442. doi:10.1016/j.biopha.2021.112442
34. Zeng M, Guo D, Fernández-Varo G, et al. The integration of nanomedicine with traditional Chinese medicine: drug delivery of natural products and other opportunities. *Mol Pharmaceut*. 2023;20(2):886–904. doi:10.1021/acs.molpharmaceut.2c00882
35. Lopez-Cantu DO, González-González RB, Sharma A, et al. Bioactive material-based nanozymes with multifunctional attributes for biomedicine: expanding antioxidant therapeutics for neuroprotection, cancer, and anti-inflammatory pathologies. *Coord Chem Rev*. 2022;469:214685. doi:10.1016/j.ccr.2022.214685
36. Zhong H, Jiang C, Huang Y. The recent development of nanozymes for targeting antibacterial, anticancer and antioxidant applications. *RSC Adv*. 2023;13(3):1539–1550. doi:10.1039/D2RA06849D
37. Bilal M, Khaliq N, Ashraf M, et al. Enzyme mimic nanomaterials as nanozymes with catalytic attributes. *Colloids Surf B*. 2023;221:112950. doi:10.1016/j.colsurfb.2022.112950
38. Ghorbani M, Izadi Z, Jafari S, et al. Preclinical studies conducted on nanozyme antioxidants: shortcomings and challenges based on US FDA regulations. *Nanomedicine*. 2021;16(13):1133–1151. doi:10.2217/nnm-2021-0030
39. Zhang R, Liu Y, Gao Y, et al. Flavonoid-rich sesame leaf extract-mediated synthesis of nanozymes: extraction optimization, chemical composition identification and bioactivity evaluation. *Food Chem*. 2024;456:140021. doi:10.1016/j.foodchem.2024.140021
40. Casals E, Zeng M, Parra-Robert M, et al. Cerium oxide nanoparticles: advances in biodistribution, toxicity, and preclinical exploration. *Small*. 2020;16(20):1907322. doi:10.1002/smll.201907322
41. Korsvik C, Patil, S, Seal, S, et al. Superoxide dismutase mimetic properties exhibited by vacancy engineered ceria nanoparticles. *Chem Commun*. 2007(10):1056–1058.
42. Lee SS, Song W, Cho M, et al. Antioxidant properties of cerium oxide nanocrystals as a function of nanocrystal diameter and surface coating. *ACS Nano*. 2013;7(11):9693–9703. doi:10.1021/nn4026806
43. Pirmohamed T, Dowding JM, Singh S, et al. Nanoceria exhibit redox state-dependent catalase mimetic activity. *Chem Commun*. 2010;46 (16):2736–2738. doi:10.1039/b922024k
44. Singh R, Singh S. Redox-dependent catalase mimetic cerium oxide-based nanozyme protect human hepatic cells from 3-AT induced acatalasemia. *Colloids Surf B Biointerfaces*. 2019;175:625–635. doi:10.1016/j.colsurfb.2018.12.042
45. Wang Z, Shen, X, Gao, X, et al. Simultaneous enzyme mimicking and chemical reduction mechanisms for nanoceria as a bio-antioxidant: a catalytic model bridging computations and experiments for nanozymes. *Nanoscale*. 2019;11(28):13289–13299.
46. Wang W, Lu, KJ, Yu, CH, et al. Nano-drug delivery systems in wound treatment and skin regeneration. *J Nanobiotechnol*. 2019;17(1):82.
47. Berthet M, Gauthier Y, Lacroix C, et al. Nanoparticle-based dressing: the future of wound treatment? *Trends Biotechnol*. 2017;35(8):770–784. doi:10.1016/j.tibtech.2017.05.005
48. Kim HS, Sun, X, Lee, JH, et al. Advanced drug delivery systems and artificial skin grafts for skin wound healing. *Adv Drug Delivery Rev*. 2019;146:209–239.
49. Hosseinzadeh R, Khorsandi, K, Esfahani, HS, et al. Preparation of cerium-curcumin and cerium-quercetin complexes and their LEDs irradiation assisted anticancer effects on MDA-MB-231 and A375 cancer cell lines. *Photodiagn Photodyn Ther*. 2021;34:102326.
50. Liu X, Ju Y, Yang P, et al. Enhanced hydrogel loading of quercetin-loaded hollow mesoporous cerium dioxide nanoparticles for skin flap survival. *Mater Today Bio*. 2025;30:101432. doi:10.1016/j.mtbio.2024.101432
51. Zeng M, Shu Y, Parra-Robert M, et al. Scalable synthesis of multicomponent multifunctional inorganic core@mesoporous silica shell nanocomposites. *Mater Sci Eng C*. 2021;128:112272. doi:10.1016/j.msec.2021.112272
52. Slita A, Egorova A, Casals E, et al. Characterization of modified mesoporous silica nanoparticles as vectors for siRNA delivery. *Asian J Pharm Sci*. 2018;13(6):592–599. doi:10.1016/j.ajps.2018.01.006
53. Li Z, Zhang Y, Feng N. Mesoporous silica nanoparticles: synthesis, classification, drug loading, pharmacokinetics, biocompatibility, and application in drug delivery. *Expert Opin Drug Deliv*. 2019;16(3):219–237.
54. McCarthy CA, Ahern RJ, Dontireddy R, et al. Mesoporous silica formulation strategies for drug dissolution enhancement: a review. *Expert Opin Drug Delivery*. 2016;13(1):93–108. doi:10.1517/17425247.2016.1100165
55. Mantina M, Chamberlin AC, Valero R, et al. Consistent van der Waals Radii for the Whole Main Group. *J Phys Chem A*. 2009;113(19):5806–5812. doi:10.1021/jp8111556
56. Abbas Z, Irshad M, Ali S, et al. Radical scavenging potential of spectrophotometric, spectroscopic, microscopic, and EDX observed zinc oxide nanoparticles from leaves, buds, and flowers extract of Bauhinia Variegata Linn: a thorough comparative insight. *Microsc Res Tech*. 2024;87 (9):2121–2133. doi:10.1002/jemt.24587
57. Summer M, Ali S, Muhammad G, et al. Evaluating the wound healing potential of characterized Bergenia ciliata –loaded salvia hispanica hydrogel in diabetic mice. *Microsc Res Tech*. 2025;88(6):1917–1934. doi:10.1002/jemt.24826
58. Popova M, Trendafilova I, Szegedi Á, et al. Experimental and theoretical study of quercetin complexes formed on pure silica and Zn-modified mesoporous MCM-41 and SBA-16 materials. *Microporous Mesoporous Mater*. 2016;228:256–265. doi:10.1016/j.micromeso.2016.04.001
59. Robaszkiewicz A, Balcerczyk A, Bartosz G. Antioxidative and prooxidative effects of quercetin on A549 cells. *Cell Biol Int*. 2007;31 (10):1245–1250.
60. Wang Y, Li C, Wan Y, et al. Quercetin-loaded ceria nanocomposite potentiate dual-directional immunoregulation via macrophage polarization against periodontal inflammation. *Small*. 2021;17(41):e2101505. doi:10.1002/smll.202101505

61. Yeni Y, Genc S, Nadaroglu H, et al. Effects of quercetin-immobilized albumin cerium oxide nanoparticles on glutamate toxicity: in vitro study. *Naunyn Schmiedebergs Arch Pharmacol*. 2025;398(5):5147–5156. doi:10.1007/s00210-024-03610-w
62. Garcia-Bennett AE. Synthesis, toxicology and potential of ordered mesoporous materials in nanomedicine. *Nanomedicine*. 2011;6(5):867–877. doi:10.2217/nnm.11.82
63. Rzigalinski B, Bailey, D, Chow, L, et al. Cerium oxide nanoparticles increase the lifespan of cultured brain cells and protect against free radical and mechanical trauma. *FASEB J*. 2003;17:A606.
64. Rzigalinski BA, Meehan K, Davis RM, et al. Radical nanomedicine. *Nanomedicine*. 2006;1(4):399–412. doi:10.2217/17435889.1.4.399
65. Heckert E, Karakoti AS, Seal S, et al. The role of cerium redox state in the SOD mimetic activity of nanoceria. *Biomaterials*. 2008;29 (18):2705–2709. doi:10.1016/j.biomaterials.2008.03.014
66. Ni D, Wei H, Chen W, et al. Ceria nanoparticles meet hepatic ischemia-reperfusion injury: the perfect imperfection. *Adv Mater*. 2019;31 (40):1902956. doi:10.1002/adma.201902956
67. Saifi MA, Sangomla S, Khurana A, et al. Protective effect of nanoceria on cisplatin-induced nephrotoxicity by amelioration of oxidative stress and pro-inflammatory mechanisms. *Biol Trace Elem Res*. 2019;189(1):145–156. doi:10.1007/s12011-018-1457-0
68. Saifi MA, Seal S, Godugu C. Nanoceria, the versatile nanoparticles: promising biomedical applicati ons. *J Control Release*. 2021;338:164–189. doi:10.1016/j.jconrel.2021.08.033
69. Sener G, Hilton SA, Osmond MJ, et al. Injectable, self-healable zwitterionic cryogels with sustained microRNA - cerium oxide nanoparticle release promote accelerated wound healing. *Acta Biomater*. 2020;101:262–272. doi:10.1016/j.actbio.2019.11.014
70. Li T, Shi S, Goel S, et al. Recent advancements in mesoporous silica nanoparticles towards therape utic applications for cancer. *Acta Biomater*. 2019;89:1–13. doi:10.1016/j.actbio.2019.02.031